



Numerical design and analysis of a multi-DBD actuator configuration for the experimental testing of ACHEON nozzle model



M. Abdollahzadeh*, F. Rodrigues, J.C. Pascoa, P.J. Oliveira

Universidade da Beira Interior, Departamento de Engenharia Electromecanica, C-MAST – Center for Mechanical and Aerospace Sciences and Technologies, FCT (Portuguese Foundation for Science and Technology) Research Unit No. 151, Covilha, Portugal

ARTICLE INFO

Article history:

Received 1 September 2014

Received in revised form 23 November 2014

Accepted 19 December 2014

Available online 30 December 2014

Keywords:

Plasma actuators

Plasma synthetic jets

Flow control

Thrust vectoring

ACHEON nozzle

ABSTRACT

Two dimensional numerical simulations of plasma actuator flow control of the ACHEON nozzle are conducted to give insight on the design of an experimental setup. Three configurations of the plasma actuators with single and multi AC-DBD actuators are used in steady mode of operation. AC-DBD actuators in standard mode (forward forcing mode), reverse mode (backward forcing mode) and plasma synthetic jets mode were used. Three different main groups of test cases were investigated by varying the reference velocity at the inlet of the nozzle stream from 4, 5 and 6 m/s. Moreover, each group includes four velocity ratios $V_R = 1, 1.5, 2, 2.5$. The locations of the flow separation points are obtained numerically for all these cases and the plasma actuators are placed slightly upstream of these points leading to a system of seven DBD plasma actuators in the forward forcing mode over the Coanda surface. The induced thrust of the AC-DBD plasma actuators was estimated using a phenomenological model which considers the maximum achieved voltage and frequency from the experiments. Using an excitation voltage with maximum amplitude of 12 kVpp and frequency of 20 kHz, ionic wind was formed with 2.4 m/s velocity. The effects of plasma actuator are presented through change of the thrust and velocity angle and thrust vectoring efficiency. Preliminary results of the experimental set-up correlate well with the numerical design values.

© 2014 Elsevier Masson SAS. All rights reserved.

1. Introduction

To maximize the agility and safety of flight missions, thrust-vectoring flight control (TVFC) is applied to complement conventional aerodynamic flight control systems. The ACHEON (Aerial Coanda High Efficiency Orienting jet Nozzle) nozzle is a novel design of thrust vectoring propulsion system without moving parts. The work is supported by European Union (Grant No. 309041) through consortium of six institutions [3].

ACHEON nozzle [14,35] makes use of two main inlet jet streams for vectoring the thrust generated nozzle. The idea is similar to fluidic thrust vectoring techniques, thus having similar advantages of being lightweight, simple and built on a fixed geometry, in comparison to mechanical thrust vectoring systems. However, the ACHEON nozzle, in contrast to traditional fluidic thrust vectoring system does not possess a secondary air jet exit and the nozzle is made up of two main primary air jets. When the velocity ratio between the primary jets is altered from unity, the exit jet of the nozzle tends to deflect toward the Coanda surface at the side of the

inlet with higher velocity. However, the thrust vectoring is limited due to separation of the boundary layer over the Coanda surfaces, which are almost entirely composed by a section of cylindrical surfaces. Flow control techniques that could suppress the separation and enhance the flow streaming over the Coanda surface, while maintaining the same functionality of the nozzle would be highly beneficial.

DBD plasma actuators [22,30] are novel means of flow control. Being fully electrical and less complex they can be easily applied in different applications for controlling flow in different situations. They have also been used and studied for controlling flow separation [20], transition to turbulent flow [28], enhancement stabilization and mixing of the flow, noise control [32], turbo-machinery flows [11,19] and other applications. However the objectives of flow control in those works are different from those in the present research, in spite of the mechanisms of controlling the flow with plasma actuators acting through the same principles. Several papers have reported the mechanism through which plasma actuators influence the surrounding flows. To improve the performance of DBD plasma actuators and their discharge behavior, different voltage shapes have been employed. However, in the aerodynamic field, two major types of DBD plasma actuators are

* Corresponding author. Tel.: +351 925467631.

E-mail address: mm.abdollahzadeh@yahoo.com (M. Abdollahzadeh).

Nomenclature

V_R	Nozzle velocity ratio	ε_0	Permittivity of space (Fm^{-1})
$f(t)$	Voltage wave form	ε_r	Relative permittivity of material
α_T	Angle of thrust (degree)	λ_d	Debye length (m)
η	Efficiency parameter	φ	Electric potential (V)
ξ	Efficiency parameters	\vec{F}_0	Body force (Nm^{-3})
T	Thrust (N)	C_{eq}	DBD actuator equivalent capacitance (F)
α_V	Angle of exit jet stream (degree)	V_{bd}	Break-down voltage (V)
V	Velocity magnetite (m)	l_p	Plasma region length (m)
y_{sep}	Y coordinate of the separation location (m)	σ	Shape factor of charge distribution
t_e	Electrode thickness (m)	μ	Shape factor of charge distribution
t_d	Dielectric layer thickness (m)	E	Electric field vector (Vm^{-1})
ε_d	Permittivity of the dielectric material	p	Static pressure (Pa)
f_{corr}	Charge density correction function	subscripts	
V_{app}	Applied voltage amplitude (V)	max	Maximum
f	Frequency of applied voltage (Hz)	*	Normalized variables
ρ	Fluid density (kg m^{-3})	v	Velocity
\vec{v}	Velocity field vector (m s^{-1})	T	Thrust
ρ_c	Charge density (m^{-3})		

currently under consideration: the Alternating Current AC-DBD and the Nanosecond DBD (NS-DBD) plasma actuators [23,33]. They differ in terms of the shape of the voltage signal that drives the discharge and, thus, the mechanism of operation. AC-DBD plasma actuations are capable of influencing the momentum boundary layer significantly in low speed regime. Therefore, they find limited application for high speed flows. As an alternative, high-voltage nanosecond pulsed DBD plasma actuators are becoming a quite attractive option for high speed applications [29,37]. The main mechanism of impact for nanosecond pulsed plasma actuators is the energy transfer [21,36]. When a DBD is excited by a nanosecond pulsed voltage, the temperature near the surface is increased (400 K for 50 ns pulse durations) [9]. Such fast heating (less than microsecond) of the gas layer leads to periodic flow disturbances that could control boundary layer.

As was mentioned before, one of the novel mean of controlling flow, and especially suppressing the flow separation, is to use surface dielectric barrier discharge (sDBD) actuators. As shown in previous studies, this kind of actuator has proven to offer great potential for flow control in different applications. The specific application we intend to demonstrate here is related to nozzles, specifically how to increase the efficiency of thrust vectoring in nozzles. Do et al. [7] used multiple DBD actuators to delay flow separation behind a bluff body in atmospheric pressure air. The bluff body was similar to Coanda surfaces of the ACHEON nozzle and was made of a flat plate connected, tangentially, to a half cylinder as a round-cornered trailing edge. The flow speed was altered in a range from 10 m/s to 25 m/s. Ginn et al. [10] patented the usage of the DBD plasma actuators for manipulating the flow in jet engine nozzles. They also suggested that the dielectric barrier discharge plasma actuators could be used to direct cooling air flow near the surface of the nozzle, thus avoiding excessive heating of the nozzle, to create thrust vectoring and reduce noise associated with the exhaust flow exiting the nozzle. Benard et al. [4–6] showed that the DBD plasma actuators could change in the deflection angle of the asymmetric jet by detaching the turbulent airflow. They have employed both steady and unsteady plasma actuators and concluded that unsteady actuation allows energizing the coherent structures and reduce power consumption while the forced jet properties are conserved. Their electrode arrangement allows production of counter-flow action on the initial region of the free turbulent shear layer.

Plasma actuators are also employed in burst mode with the applied voltage being duty cycled with a specified burst frequency and burst ratio. Kopiev et al. [18] conducted an experimental study on the effect of high frequency DBD actuator on nozzle exit jet. They claimed that the plasma actuator effect is related with the acoustic radiation of the discharge, and showed that jet noise suppression and intensification were achievable depending on the jet excitation frequency. Kim et al. [16] and Samimy et al. [25] used localized arc filament plasma actuators (LAFPA) which were powered by a pulsed radio frequency (RF) plasma generator for flow control of a high speed circular jet. These arc plasmas were shown to be capable of flow excitation by depositing energy at fast rate in the flow. The principles are similar to addition of energy and micro shock wave generation due to nano-second pulsed DBD plasma actuators [1]. Kleinman et al. [17] demonstrated numerically the control ability of LAFPA to alter the development of supersonic turbulent jets and suppress their noise. Recently, Das et al. [31] showed that multiple electrode configuration of plasma actuators is effectively capable of changing the exit jet flow direction. In the continuation of these studies, we will in this paper consider the application of DBD plasma actuator to improve the ACHEON nozzle thrust vectoring efficiency.

As a part of ongoing research in ClusterDEM lab [12], the experimental facilities were prepared for testing the ACHEON nozzle geometry with plasma actuators [24]. The schematic of the experimental setup is shown in Fig. 1. However, due to limitation of the achievable voltage, the controlling effect of one single AC-DBD actuator is restricted. The objective of the present work is to design a single or multi AC-DBD actuator configuration capable of controlling the flow in the ACHEON nozzle. The design output should include the position of the electrodes and number of DBD pairs. The procedure is limited by the available experimental facility, namely the maximum excitation voltage and frequency and the experimental inlet velocities.

2. Presentation of the ACHEON nozzle

The dimensions of the ACHEON nozzle model are presented in Fig. 2. The Coanda surfaces are sections of cylindrical surface made of 2 mm thick polycarbonate sheet. The two main primary jets where created by using two electric ducted turbfans (EDTs) at the inlets with diameter of 70 mm.



Fig. 1. Experimental test setup for controlling flow of ACHEON nozzle with plasma actuators.

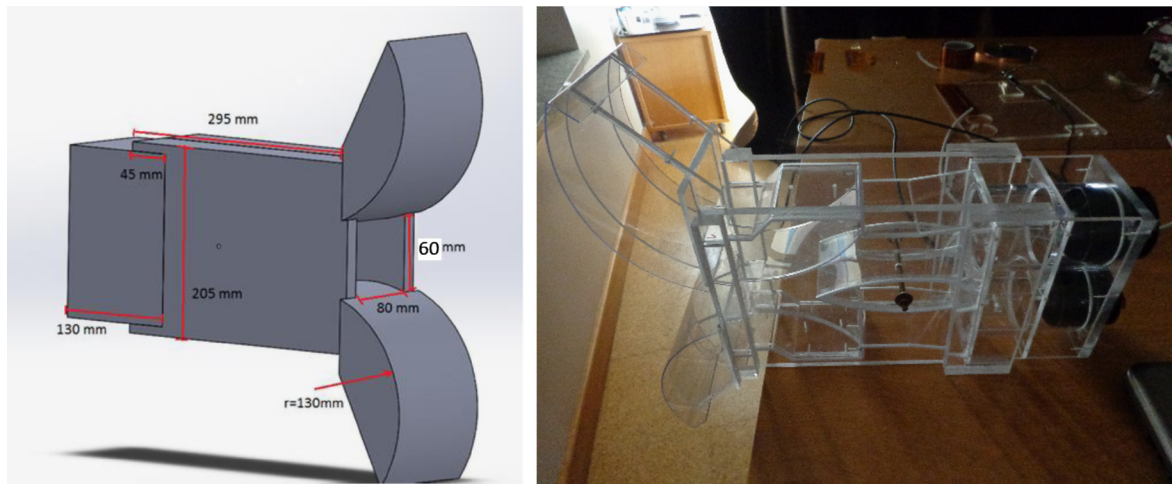


Fig. 2. Dimensions of the ACHEON nozzle.

Previous studies have shown that the control authority of the DBD actuators is dependent on their position in particular for the case of suppressing separation; the best functionality will be achieved when the actuator is placed slightly before the separation point [15]. Thus, to correctly define the position of the DBD actuators, the velocities at the inlet of each stream are required for the computation of the flow field and the locations of low separation on the Coanda surfaces. According to the available experimental facility, three different test cases were selected, see Section 4.

3. Governing equations and numerical procedure

CFD simulations of the flow field without the DBD actuator were done initially to obtain the necessary data for designing the experimental setup. For simplicity, a 2D computational domain was considered by ignoring three dimensional effects and the numerical grid used for the simulation is presented in Fig. 3.

The initial simulation was performed with the Commercial CFD solver FLUENT by discretizing the governing equation with finite volume method (FVM) using a cell centered collocated arrangement of primitive variables. For this purpose, the steady two dimensional (2D) incompressible Reynolds-Averaged Navier–Stokes (RANS) equations were solved with a coupled solver. The second order upwind scheme was used to discretize the convective terms, and the $k-\omega$ SST model was employed for modeling turbulence. Moreover, the interaction of the plasma actuator is implemented as an explicit source term inside the momentum equation. A simple phenomenological model developed by Abdollahzadeh et al. [2]

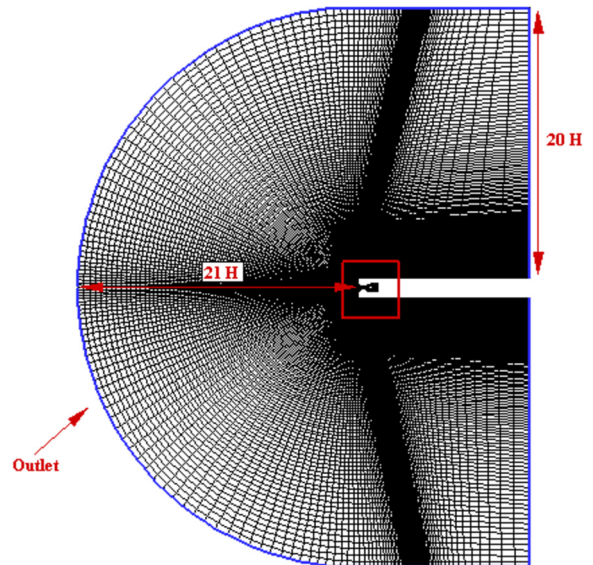


Fig. 3. 2D computational mesh (328 000 grid cells).

was used for modeling the plasma actuators effect. This model is based on correct scaling of the plasma generated thrust for computing the body force and provides the distribution of the body force vector field. Moreover, assuming that, the characteristic time scale of plasma is much smaller than the time scale of the flow,

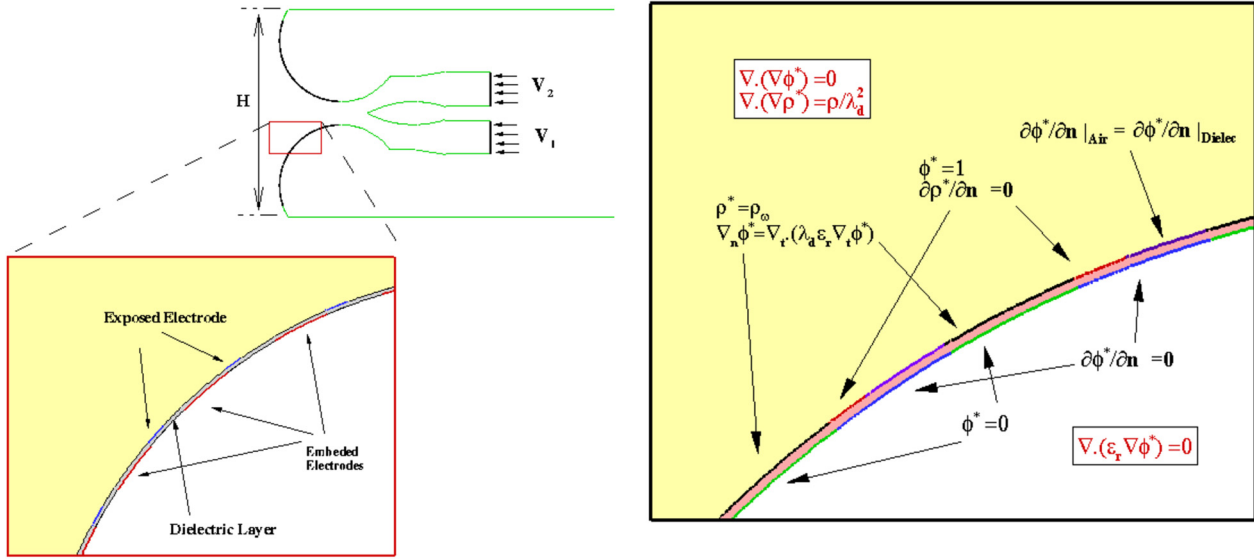


Fig. 4. Normalized boundary condition of the plasma model applied to compute the DBD induced force.

an averaged body force distribution during a cycle period is used to model the effect of DBD plasma actuator. The governing equations of flow and the plasma model (electric potential and charge density) are as follows:

$$\text{div}(\rho \vec{v}) = 0, \quad (1)$$

$$\text{div}(\rho \vec{v} \vec{v}) = -\nabla p + \nabla \cdot (\tau) + \vec{F}_0 \quad (2)$$

$$\nabla \cdot (\epsilon \nabla \varphi^*) = 0, \quad (3)$$

$$\nabla \cdot (\epsilon_r \nabla \rho_c^*) = \frac{\rho_c^*}{\lambda_D^2}, \quad \epsilon = \epsilon_0 \epsilon_r \quad (4)$$

where

$$\vec{F}_0 = \rho_c \vec{E} \quad (5)$$

$$\rho_c^* = \frac{\rho_c}{\rho_{c,\max} f(t)}, \quad \varphi^* = \frac{\varphi}{\varphi_{\max} f(t)},$$

$$\vec{E}^* = \nabla \varphi^* = l_p \left(\frac{\partial \varphi^*}{\partial x} \vec{i} + \frac{\partial \varphi^*}{\partial y} \vec{j} \right), \quad (6)$$

$$\rho_{c,\max} = 2f C_{eq} \frac{(V_{app} - V_{bd})}{f_{corr} \lambda_d},$$

$$f_{corr} = \frac{1}{2} \sqrt{2\pi} \frac{\sigma}{l_p} \left[\text{erf}\left(\frac{1}{2} \frac{\mu \sqrt{2}}{\sigma}\right) + \text{erf}\left(\frac{1}{2} \frac{\sqrt{2}(l_p - \mu)}{\sigma}\right) \right] \quad (7)$$

$$\vec{E} = E_0 \vec{E}^* \quad E_0 = \frac{(V_{app} - V_{bd})}{l_p} \quad (8)$$

In the above equations $f(t)$ is a function representing the shape of the applied voltage and \vec{E}^* is the normalized electric potential. In the above described model, a Gaussian distribution of charge density is considered over the dielectric surface,

$$\rho_{c,w}^*(t) = \frac{\rho_{c,w}(t)}{f(t)} = \rho_{c,\max} \exp\left(-\frac{(s - \mu)^2}{2\sigma^2}\right) \quad (9)$$

where s is the length of the surface. Once the dimensionless distribution is determined, the dimensional values at any given time can be obtained by multiplying this distribution with the corresponding normalization factor. In this manner, there is no need to solve the plasma model in an unsteady manner. The corresponding normalized boundary conditions of the plasma model are presented in Fig. 4 for the DBD actuator geometry.

The plasma model was then coded as a UDF (User Defined Function) and was used alongside for the simulation purpose. We note that the grid spacing should not be larger than the Debye length and the condition $y^+ < 1$ where $y^+ = \frac{u^+ y}{\nu}$ must be satisfied for correctly resolving the development of the turbulent boundary layer. For enforcing these conditions and reaching grid independence of the results at reasonable numerical cost, the grid was refined toward the electrodes and surface of dielectric layer. Moreover, the grid was refined in the regions where higher values of electric field and charge density exist. Hence, the grid spacing was stretched toward the electrode both in the normal direction and in the streamwise direction, thus leading to minimum cell size of about 2 μm .

At the inlet of the nozzles, the velocity magnitude and direction are prescribed alongside with turbulent intensity and turbulent viscosity ratio. At the walls, the no-slip boundary conditions are used. The boundary representing the outlet is considered to be far enough from the exit of the nozzle (as shown in Fig. 3). Pressure outlet boundary condition was used at this boundary by assigning the value of the static pressure and turbulent intensity (0.1%) and viscosity ratio. It is true that at the inlet there should be high levels of turbulence. As this is the case, because of high level of turbulence at the inlet, the transition is bypass type, and most of the turbulence models do not capture it accurately. However, the purpose of this investigation is only to analyze the Coanda flow separation. Therefore, we have assigned low turbulent intensity values to avoid bypass transition. Although this is not the probably true case of experiments, we wanted to make sure that bypass transition was not observed prior to flow separation. Thus the flow will be laminar before separation and turbulent after separation.

Moreover, the k - ω SST model used here is one of the best for near wall and separational flows. Study of the influence of turbulent intensity on flow deflection will be the subject of future work.

4. Description of the experimental set-up

In the experiments, two turbofans HET EDF 6904 were used to produce the two inlet flows to the nozzle. The turbofans contain brushless motors Typhoon EDF 4W and were controlled with electronic speed controllers 80A-Eco-6S ESC and pulse generators PWM Hobbyking LED Servo Tester. The DBD plasma actuators were fed by PVM 500, that is a high voltage frequency power supply,

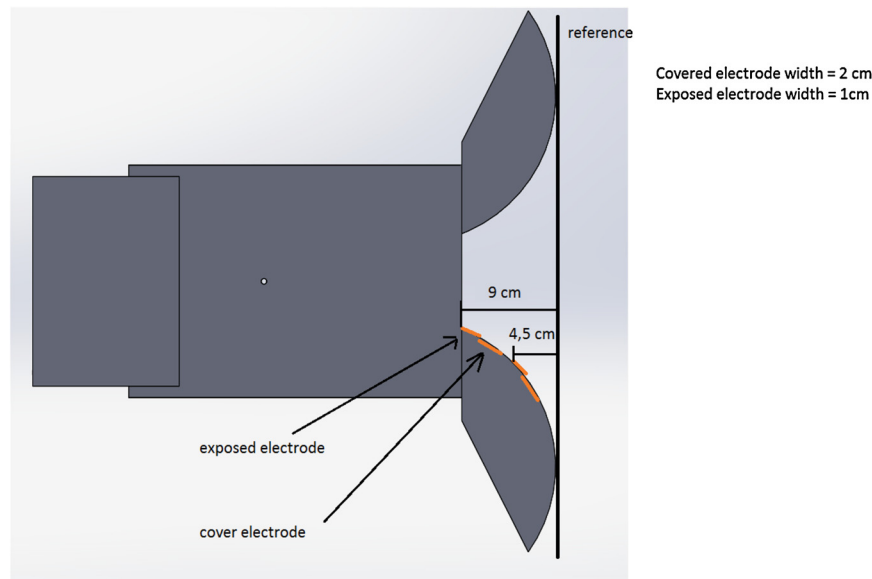


Fig. 5. Schematic of the configuration of the DBDs in experiments.

and the voltage waveform was produced by PWM 500 and measured with digital oscilloscope software designated by PicoScope. Together with the PicoScope, was used an accessory designated by Secondary Ignition Pickup allowed us measure the voltage and the frequency of the signal. A laser sheet and a digital camera CCD C10600-10B Orca-R2 was used to visualize the flow field. The laser used was a 1 L2S-SL-660-130-S-A-60 SteamLine Laser System and it can work in a continuous mode or in a pulse mode. It was feed with 5 V and 250 mA by a power supply ITT Instruments AX 322 Metrix. Solid particles were seeded uniformly using a cyclone particle generator at the turbofans intakes. The cyclone particle generator contains an inlet where compressed air is introduced and an outlet to exit the mix of air and solid particles. Talcum powder was used to mark the flow once the talcum particles can follow the flow without change its properties and present a good reflection of the incident light. Before starting the experiments a compressor with 110 L reservoir was used to compress and store the air at a pressure of about 8 bar and the talcum powder was deposited in the base of the solid particle generator. The digital camera CCD C10600-10B Orca-R2 was positioned perpendicularly to the laser sheet and connected to the computer. The configurations of the capture and the reception of the images were done using the software HCLImage Live. The schematic of the experimental set-up is shown in Fig. 1.

To make a PIV analysis and to acquire a pair of images with a very small time interval between them, the PIV mode of the camera was used which allows the capture of two consecutive images taking only 2 μ s from the end of the first exposure until the beginning of the second exposure. This operation mode of the camera requires the control by an external TTL signal and to produce it, a signal generator was used. Then a square signal with 5 V of amplitude and about 6 kHz was created with the signal generator. At an input trigger signal edge (rising or falling edge), the camera starts the acquisition of one image pair. As the frequency of the external signal is very high, the camera captures consecutive acquisitions of image pairs until reaching the number of images defined by the user. Before starting the acquisition of image pairs, one calibration image was captured in order to define the relation between the pixels of the image and the metric scale. After the acquisition of the image pairs the software PIVLab was used to make the PIV analysis and obtain the velocities of the flow. The final result of the PIV measurement was obtained by the average values of 10 PIV measurements. These ten PIV measurements were

performed for ten consecutive image pairs. The exposure time of each image was 100 μ s but the time between each image pair was 60 ms. The images of the flow visualization were captured with 60 ms of exposure. To measure the deflection angle a reference point was defined for all the images. The reference point was located at 67 pixels from the left side of the image and 519 pixels from the top of the image. Lines were drawn from the top of the flow until the bottom of the flow and the middle point of these lines was calculated. These lines were drawn at a distance of 400, 700 and 1000 pixels from the left side of the image and the angle was measured between the reference point and each of the middle points of the lines.

The position of the DBD actuator sets used in the experiments is shown in Fig. 5. The width of the covered electrode is 2 cm and the width of the exposed electrode is 1 cm. In Table 2, we give some of the basic information about the DBDs available in the experiments. The dielectric material was made from a 2 mm polycarbonate layer, electrodes were made from 0.1 μ m copper tape. An AC-sinusoidal voltage with 12 kVpp and 20 kHz was used as an excitation voltage.

5. Results and discussion

The ACHEON nozzle was tested with simulations based on the values of the velocity magnitude at the inlet of the nozzles given in Table 1. When the velocity ratio is equal to unity, the jet out of the nozzle and the induced thrust are horizontal. This is considered the base case for comparing the capabilities of the plasma actuators for thrust vectoring. When the velocity ratio is increased, the jet at the exit starts deflecting towards the Coanda surface at the inlet side having higher velocity magnitude. For each case, we are interested on the following results: the location of separation point; maximum velocity at the nozzle (V_{max}), the thrust (T), the angle of thrust generated at the nozzle (α_T); and angle of the exit jet stream of the nozzle (α_V). Table 1 gives the data calculated by the numerical simulation. For comparing the vectoring capability, two parameters are considered, the induced thrust angle and the exit jet angle. It is possible to define efficiency parameters based on these angles and the mass flow rates at the inlet of nozzles as follows:

$$\eta_T = \frac{\alpha_T}{(\frac{\dot{m}_1}{\dot{m}_1 + \dot{m}_2})} \quad (10)$$

Table 1
Input and output data for the nozzle flows without plasma actuators.

V_R	V_1 (m/s)	V_2 (m/s)	T (N)	V_{\max} (m/s)	α_V (degree)	α_T (degree)	Y_{sep}
Test 1							
1	4	4	4.14	12.19	0	0.00	−0.0284
1.5	4	6	7.63	17.23	21.01	26.21	−0.0411
2	4	8	12.80	21.68	30.22	33.52	−0.0520
2.5	4	10	19.80	25.86	38.41	37.51	−0.0640
Test 2							
1	5	5	6.26	15.23	0	0.00	−0.0289
1.5	5	7.5	12.02	21.54	22.68	27.97	−0.0434
2	5	10	21.09	27.08	34.43	35.46	−0.0581
2.5	5	12.5	37.92	32.34	52.87	38.75	−0.0884
Test 3							
1	6	6	8.77	18.27	0	0.01	−0.0290
1.5	6	9	17.79	25.85	25.11	30.21	−0.0466
2	6	12	31.95	32.44	37.86	36.83	−0.0643
2.5	6	15	58.13	39.01	63.98	38.67	−0.1006

Essentially, to insure a secure flight mission when using ACHEON for aircraft propulsion, a safety angle (maximum desirable design angle) for the thrust vectoring purpose needs to be defined. Here, arbitrarily, we assume that the thrust safety angle should be equal to 45 degrees. This angle depends in a complex way on the flight speed, thrust magnitude, weight and size of the system. Considering this value we can reformulate Eq. (10) as follows:

$$\xi_T = \frac{2\alpha_T}{45(V_R + 1)} \quad (11)$$

$$\eta_T = 1 - 2 \frac{|\alpha_T - 45|}{45} \frac{1}{(V_R + 1)} \quad (12)$$

The detailed numerical results obtained by the simulations are presented in Table 1. It is clear that when the velocity ratio between nozzle inlets increases, the deflection angle of the jet is increased. However, the thrust angle increment is not at the same rate as the angle of the exit jet. It should be reminded that this improvement in vectoring capability is obtained by spending more power in comparison to the case of $V_R = 1.0$. The position of separation point was also calculated for different cases and presented in Table 1. These results show that flow separation over the Coanda surface is postponed when the velocity ratio is increased. This enhanced tendency of the flow to follow the surface curvature could be ascribed to enhanced injection of momentum from outside the boundary layer to zones with lower velocity magnitude, because of the difference of pressure drop between the two inlet jet stream sections.

In Fig. 6, the velocity contours of the ACHEON nozzle are shown for various velocity ratios, for the first test case. These figures illustrate how with an increase in the velocity ratio, higher deflections of the exit jet angle are achieved. Moreover, by comparing the results for the three test cases indicated in Table 1 (low, medium and high velocity range), it is possible to conclude that, when the inlet velocity magnitude is increased, the deflection angles for thrust and velocity become larger, but the thrust angle reaches its maximum possible value (imposed by design and geometrical limitation) sooner.

In Fig. 7, the velocity angle at the exit of nozzle, the thrust angle and the performance ratios (Eqs. (10) and (11)) are plotted for different velocity ratios. The results clearly point out the existence of a limiting thrust angle for the considered dimensions of the ACHEON nozzle. As can be seen, the plot of thrust angle versus velocity ratio meets a plateau at a maximum angle of around 39 degrees. It may also be observed that, when the nozzle exit velocity magnitude is increased (going from Test 1 to Test 3), the limiting thrust angle occurs at lower velocity ratios. However, the velocity angle is seen to increase almost constantly over the ve-

Table 2
Operating conditions.

t_e	0.1 μm
t_d	2 mm
ϵ_d	3.1 polycarbonate
V_{app}	6 kV
f	20 kHz
T	293.15 K

locity ratios here tested. We see that this does not always imply increase in the thrust vectoring capability.

The experimental facility of our lab provides us with a specified range of operating conditions that need to be considered for the design of the DBD system. Table 2 presents the power source characteristic, the thickness of the available electrode, thickness of the dielectric material and permittivity of the dielectric material.

For the problem under consideration here, the previous CFD results showed that when the velocity ratio of the nozzle is increased, the separation point varies. Thus to design a flow control system based on DBDs able to act almost universally over the whole duration of a flight mission (velocity ranges and velocity ratios), a multi-DBD actuator system should be adopted taking into consideration the location of the various flow separation points. That is, for global functionality, a DBD actuator is positioned at each major separation point, and the distance between separation points is covered by the length of each DBD actuator system. Since each actuator can operate separately, there should be enough space between the electrodes of each system for preventing arc and short-circuit formation. Therefore we consider seven sets of actuator, with 15 mm length embedded electrode and 6 mm exposed electrodes.

Previous results have shown that the influence of the DBDs on each other is additive, and our CFD results [39] revealed that the multi-DBD system will cause ionic wind with higher intensity. To confirm this and to better understand how a multi-DBD actuator is more effective than a single DBD actuator, Fig. 8 shows simulation results for the ionic wind of a single DBD set and for a multiple DBD set (four actuators). The maximum ionic wind induced by the multiple DBD is clearly greater than with the single DBD case and the plasma wall jet is seen to cover a much larger controlling surface area.

For the purpose of comparing the effect of actuator location and number of active DBDs, a series of numerical tests have been carried out. To limit the number of cases to be studied, we have considered one active DBD (seven test cases indicated from E1, DBD at the beginning of the Coanda surface to E7, DBD near to the end of the trailing edge of the Coanda surface), two active DBDs in row (six test cases, E12 to E67, with numbers showing the location of the DBDs), three active DBDs in row (five test cases, E1-3

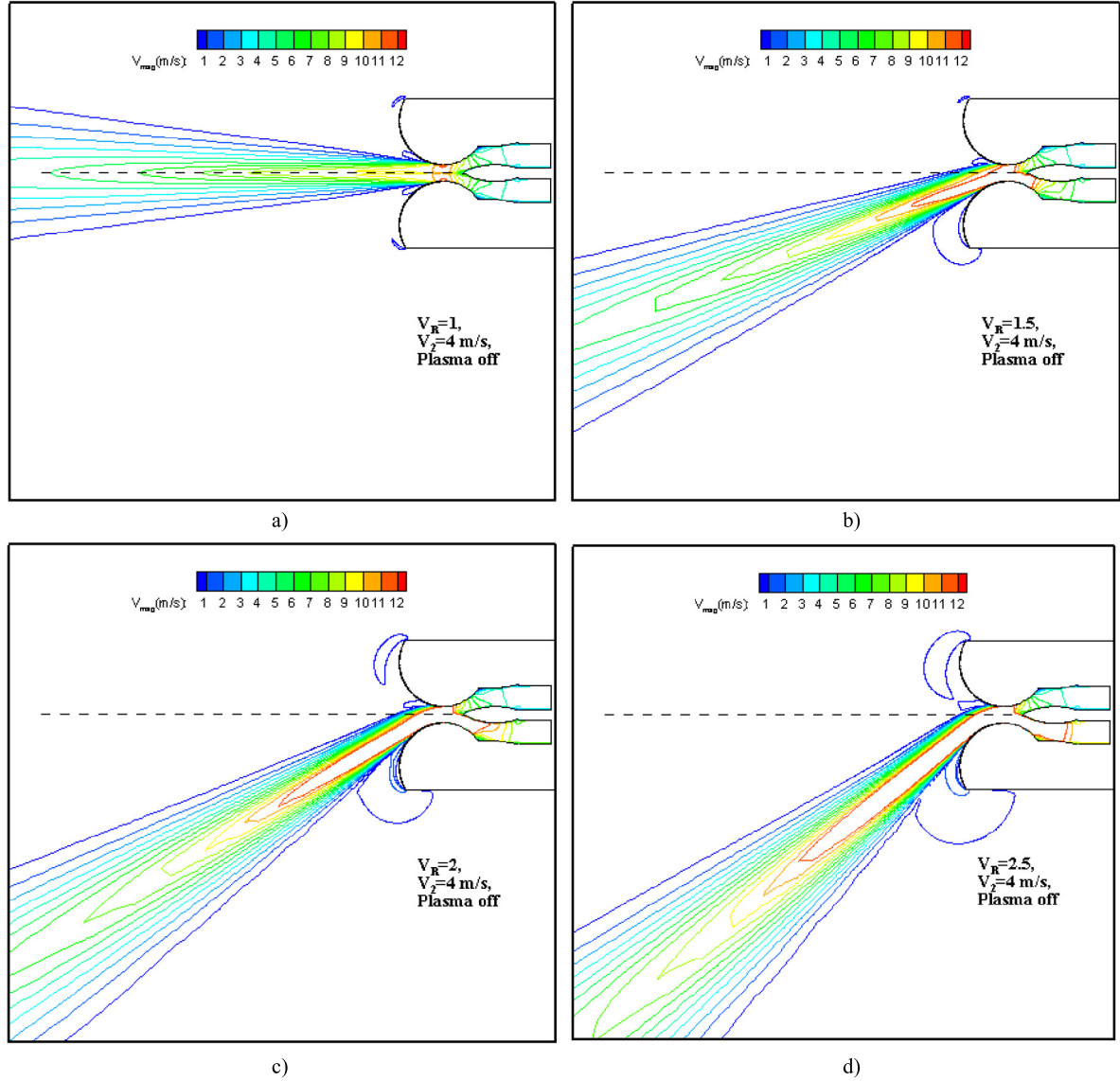


Fig. 6. Velocity contour at the exit of the nozzle at a) $V_R = 1.0$, b) $V_R = 1.5$, c) $V_R = 2.0$, d) $V_R = 2.5$ (all cases with $V_f = 4$ m/s).

to E5-7) and also four cases with four to seven active DBDs (E1-4, E1-5, E1-6, E1-7). We considered the velocities equal to the condition of Test 1. Fig. 9 shows the comparison between these cases for different values of velocity ratios. The dependency of the actuation efficiency is clearly obvious from this figure. When the actuation zone is located slightly before the separation point, the plasma actuators have effective performance on controlling the flow. Actuators E6 and E7 which are installed at the end part of the Coanda surface, do not have any effect on the flow characteristic. Thus in the case of single active actuator depending on the velocity ratio, one of the actuators from E2 to E5 should be turned on. It is possible to increase the tolerance of controlling algorithms by using two sets of side by side active actuators. In this case, for each velocity ratio (except $V_R = 1$), there is two possible selections for the active actuator set. Moreover in this case, we observe that, the velocity deflection angle is improved for all velocity ratios (in $V_R = 1.5$ it wasn't significant). When three side by side DBDs are active, the controlling effect is improved. The number of possible configurations which can be used for flow actuation also increases. In Fig. 9d, more than four DBD sets are active. Difference between E1-6 and E1-7 are almost negligible and, when $V_R = 1$ and 1.5, all the cases show almost the same efficiency. However, when the ve-

locity ratio is increased, especially at $V_R = 2.5$, the arrangements that cover greater part of the Coanda surface have larger performance. However, when the numbers of electrodes are increased the total power consumption will increase.

It is interesting to mention that, it was possible to alter the velocity angle by at least 10 degrees by altering the active DBD location. In Fig. 10, velocity contour corresponding to the selected cases at $V_R = 2.0$ and with single and double DBDs are shown. When single DBD is used, by using an actuator at E5 the velocity angle just changes around 31.85 degrees. Changing the position of the DBD to E3 and E4 causes the thrust angle to increase respectively to 34.3 and 38.1 degrees. This is quite interesting, since if one covers the suit surface with a suitable number of actuators, and using a suitable control algorithm, it will be possible to alter the flow angle arbitrarily with less power consumption.

In Fig. 11, the thrust vectoring performance number and efficiency, for different configurations of DBD plasma actuators, and nozzle velocity ratios, are shown. η_T and ζ_T are showing the point for optimum thrust vectoring on different velocity ratios. However, both variations show that maximum thrust vectoring occurs at medium velocity ratios. This result can be justified by the fact that, at higher velocity ratios, boundary layer is already attached

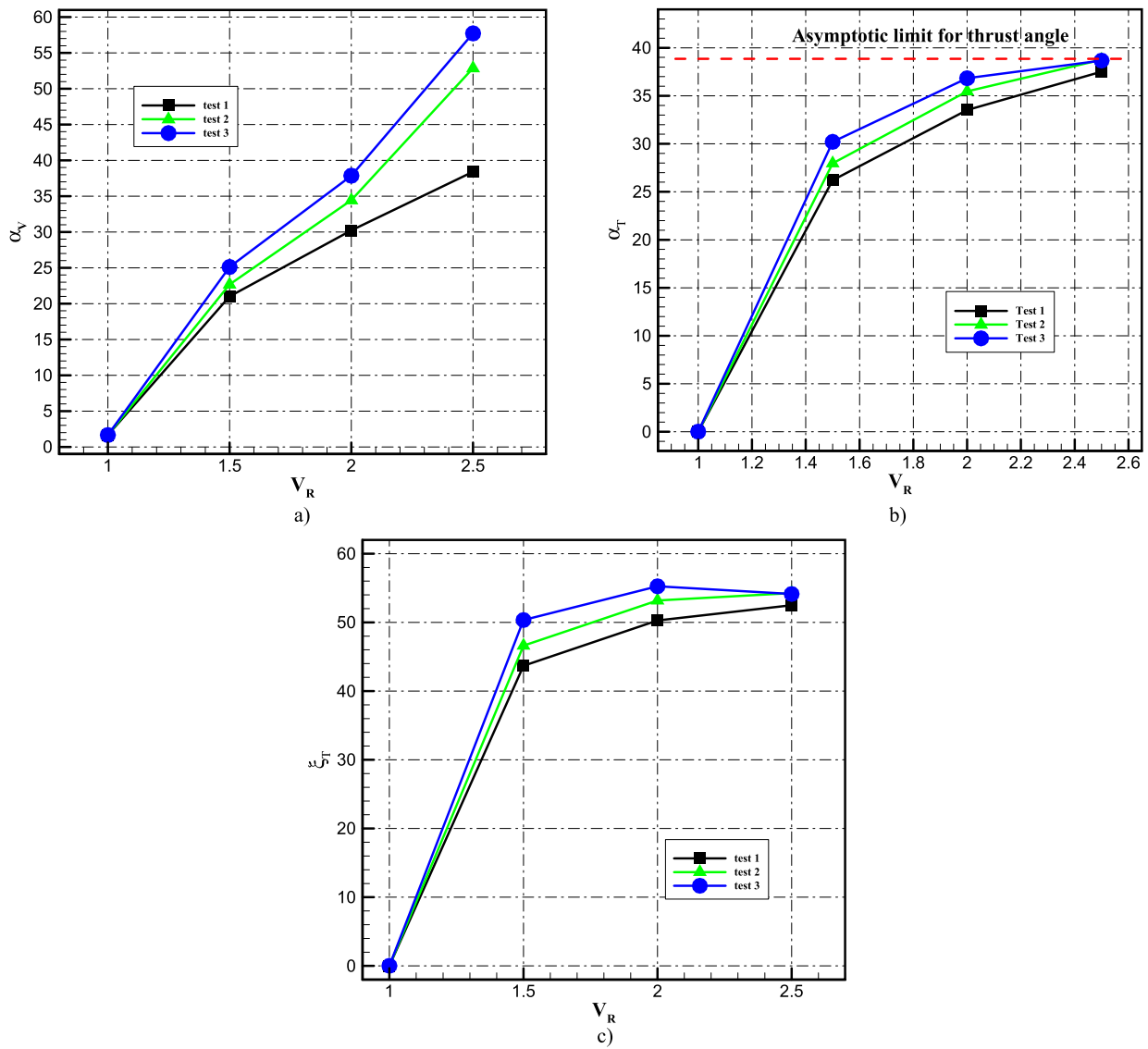


Fig. 7. Results of the simulations without plasma actuators for increasing velocity ratios of $V_R = 1, 1.5, 2, 2.5$. a) Angle of the jet deflection. b) Angle of the thrust vector. c) Thrust vectoring performance number.

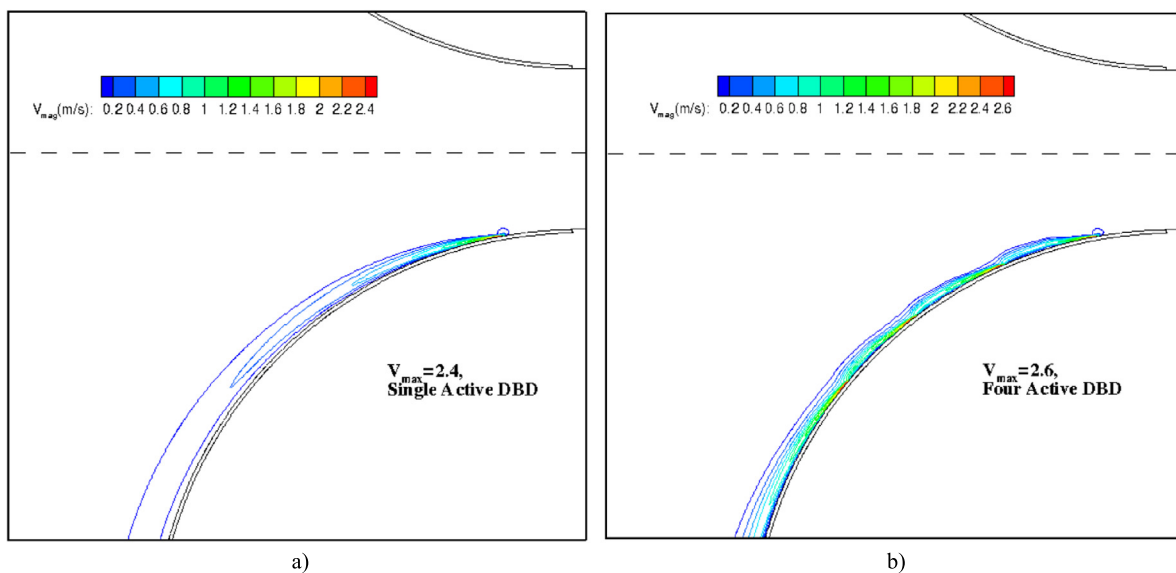


Fig. 8. Induced ionic wind: a) single DBD actuator; b) multiple DBD actuators.

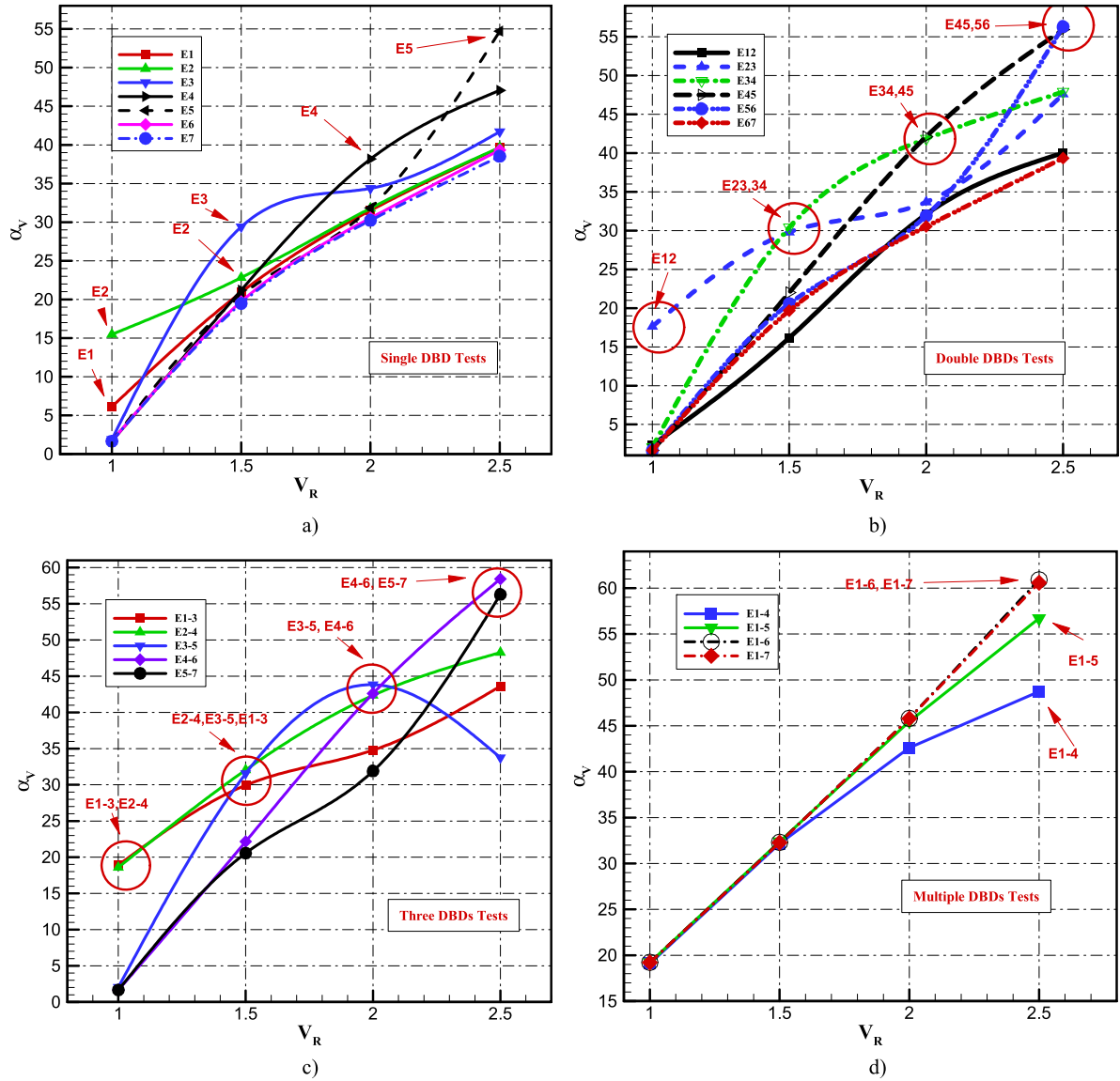


Fig. 9. Effect of DBD plasma actuator on exit jet angle from the nozzle: a) single DBD actuator; b) two DBD actuators; c) three DBD actuators; d) multiple DBD actuators.

to the Coanda surface to the maximum extent (look at asymptotic value of thrust), thus further increasing the velocity ratio or using plasma actuators would not add more efficiency to the system but it will use more power.

In Tables 3 and 4, the flow and thrust deflection angles are tabulated for all the cases with plasma actuators. As can be seen if the plasma actuator is placed at optimum location, the increment in the velocity vectorizing is large, from 16.5 degrees for single actuator to 23.39 degrees for multiple DBDs. We should mention that this increment will be reduced when the velocity magnitude at the inlet of the nozzle is increased. However, by analysis of the data of thrust angle, we see that the influence of DBD system on thrust vectorizing is just pronounced at low velocity ratios and even in the presence of single or multiple DBD actuators the thrust angle will not increase more than its asymptotic value, shown in Fig. 7b. Moreover, we should mention that, the increment in thrust angle at those cases that DBD is installed at exit section of the Coanda surface is not related to increase in Coanda effect for suppression of separation over the surface. It is only related to the surface jet created by the plasma actuator (here with 2.4 m/s speed).

Besides the standard configuration of the actuator that was shown with single and multiple DBDs, plasma actuators can be

used in several different configurations [8,13,18,27,38]. Here, using 2D modeling we only consider two of these configurations. In the first case, a plasma actuator is added in the top Coanda surface in a reverse mode to promote separation of the jet stream earlier. In the second case, linear plasma synthetic jet actuators [26] (two plasma actuators, one acts in forward mode and other acting reverse mode) are placed over the top surface to induce a jet normal to the surface. In Fig. 12 the induced ionic winds of the plasma actuator for the mentioned configurations in quiescent air are presented.

The velocity contour corresponding to the cases with single and multiple (two) DBD actuators in reverse mode and single and double DBD plasma jets are shown in Fig. 13. These results are for the velocity ratio equal to unity with the inlet velocity of 4 m/s. When the actuator is used in reverse mode on the top Coanda surface, the separation is promoted and exit jet of the nozzle is deflected downward. Using multiple DBD actuators also increases the deflection of the jet. Interestingly, when DBD plasma jets are used, the flow tends to be directed upwards.

To verify the accuracy and validity of the numerical simulation, basic PIV measurements of the exit jet of the nozzle were used for measuring the average velocities, as shown in Fig. 14 for validat-

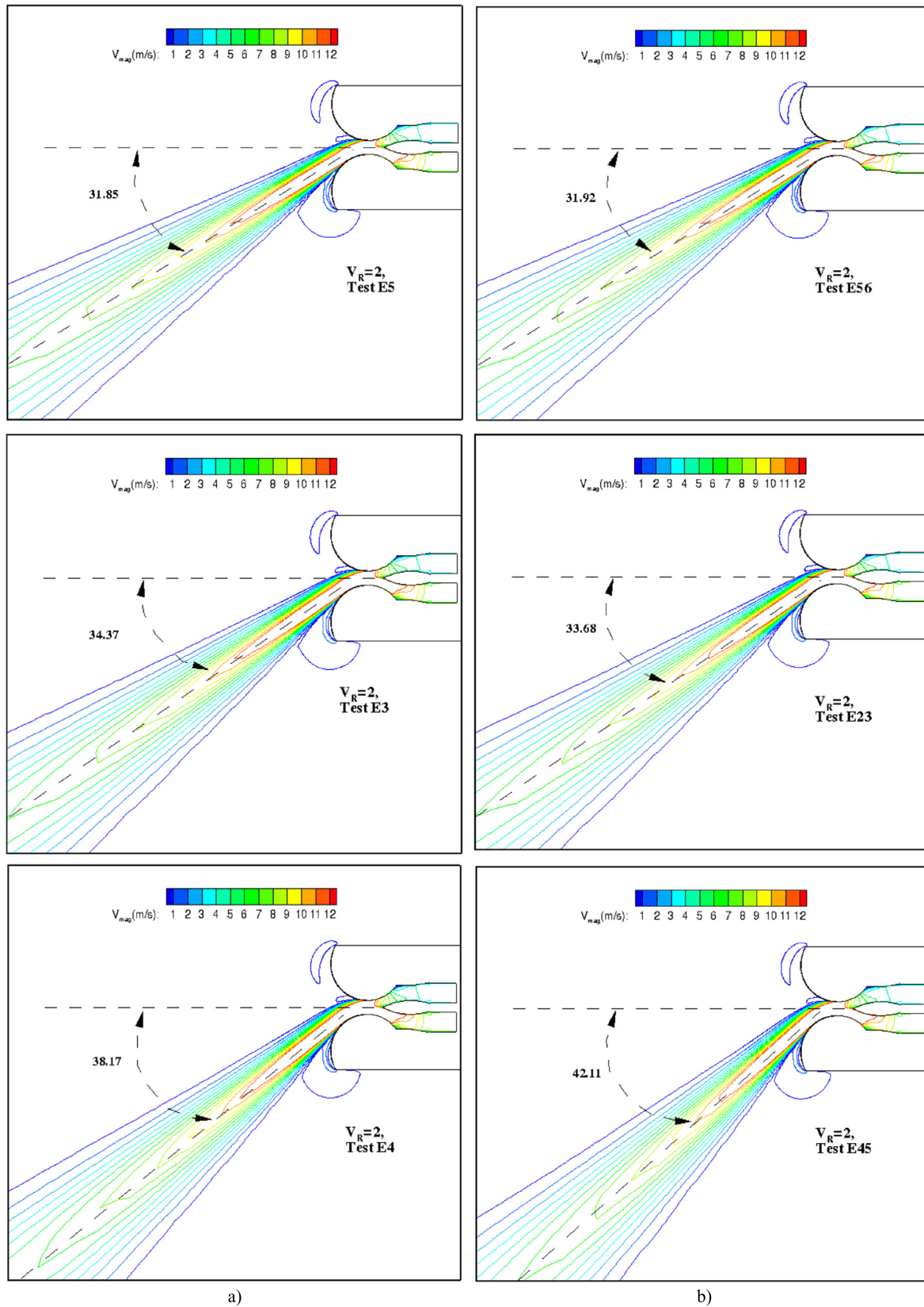


Fig. 10. Effect of DBD plasma actuator on direction of the exit jet of the ACHEON nozzle: a) single DBD; b) double DBD.

ing the baseline flow. The PIV measurements were conducted for $V_R = 1$ and $V_2 \approx 2$ m/s. The average velocities in five velocity profiles are tabulated and are compared with numerical simulation in Table 5. The small differences between the numerical and exper-

imental results are related to the fact that the numerical results are a 2D approximation of the 3D experiments. Moreover, the imposed boundary conditions in the numerical simulations V_1 and V_2 are pure axial velocities. However we have computed before

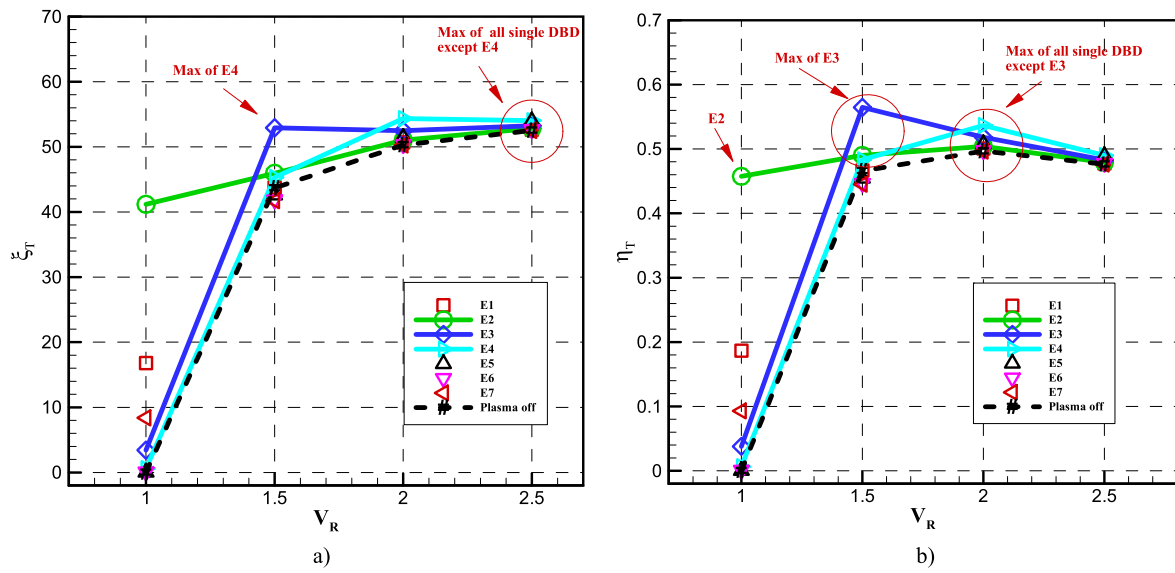


Fig. 11. Effect of DBD plasma actuator on a) thrust vectoring efficiency, b) thrust vectoring performance number.

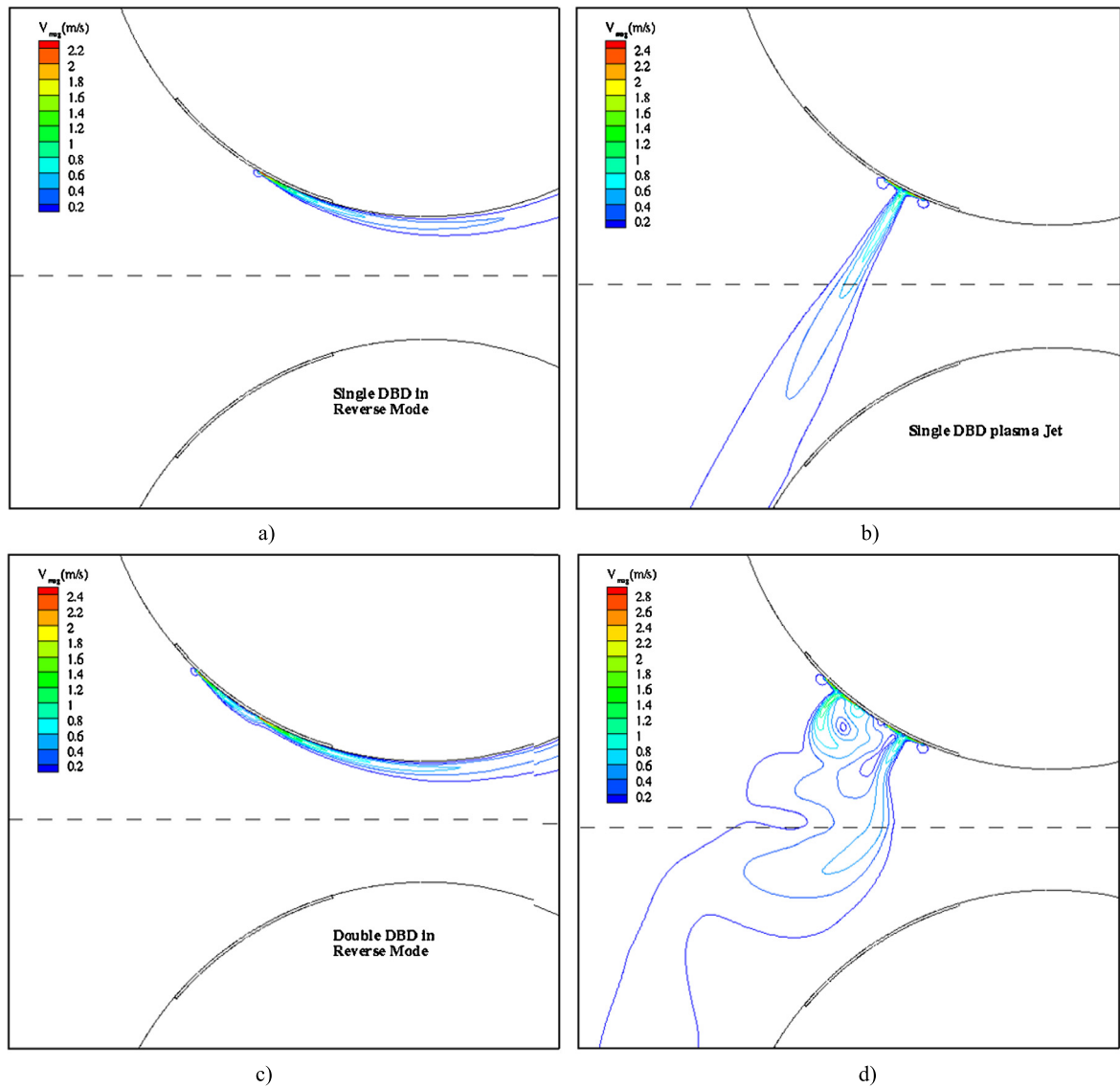


Fig. 12. Velocity contours of the induced ionic wind of a) single reverse actuator, b) single DBD plasma jet, c) multiple reverse DBD actuators, d) multiple DBD plasma jets, installed on the top Coanda surface.

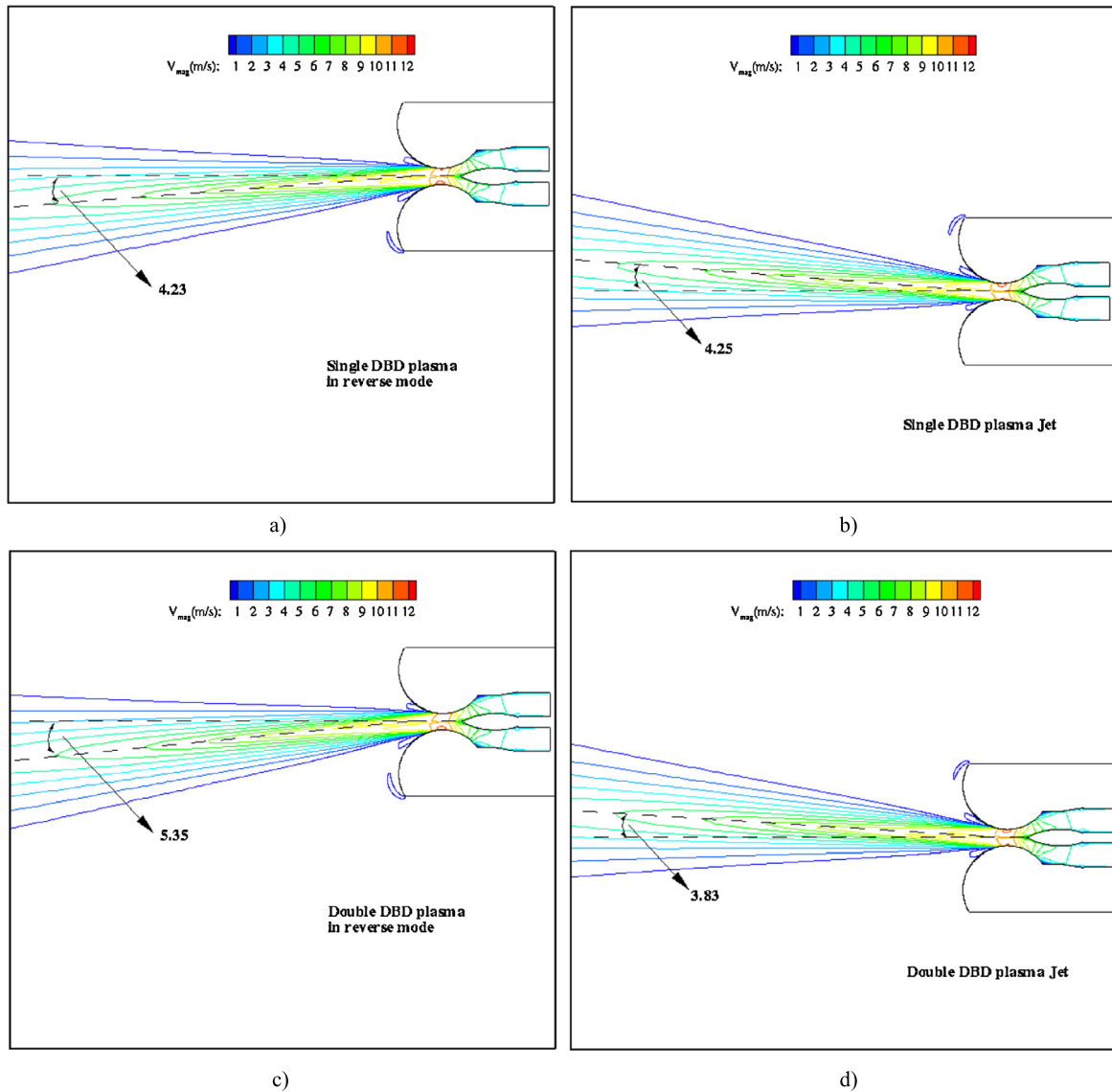


Fig. 13. Velocity contours at the exit of the ACHEON nozzle with a) single reverse actuator, b) single DBD plasma jet, c) multiple reverse DBD actuators, d) multiple DBD plasma jets, installed on the top Coanda surface.

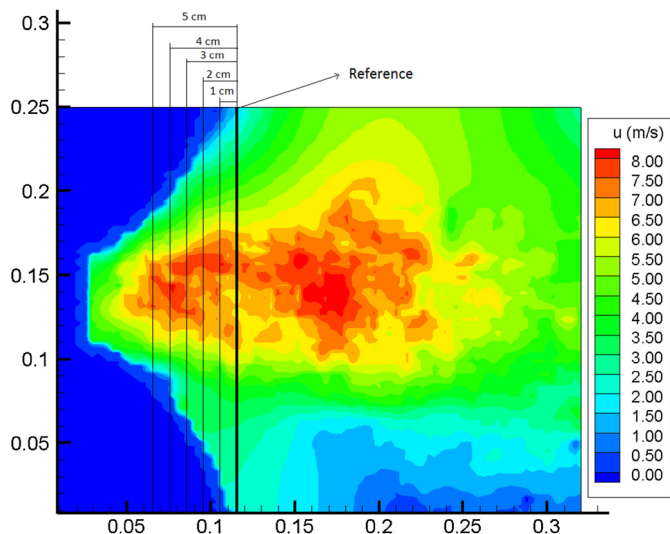


Fig. 14. PIV results of exit jet of the nozzle without DBD.

that swirl velocity induced by the two fans reduces the velocity vector exit angle. In the 3D experiments the flow, after exiting the nozzle starts to spread towards the lateral areas, thus the velocity level in that regime should be lower than the computed by 2D numerical simulation.

We should note that PIV computes instantaneous velocity fields and a large number of PIV results are needed to achieve an asymptotic averaged solution, for the velocity field obtained experimentally to be comparable with averaged results of CFD computation. We should note that due to difficulty in the experiments and high levels of unsteadiness, obtaining a perfectly averaged solution was difficult.

From the preliminary result of the experimental tests, the jet deflection angle was calculated by analyzing more than 20 images for the cases with the actuators off and on, in order to decrease the error of the measurement. The jet angle is calculated by defining the potential core center of the jet. This center is defined as the mean distance between the upper and lower shear layers. In Fig. 15, for the purpose of conciseness, only three consecutive snapshots of the air jet are plotted for both the uncontrolled case and the controlled case. According to Taylor [34], the uncertainty

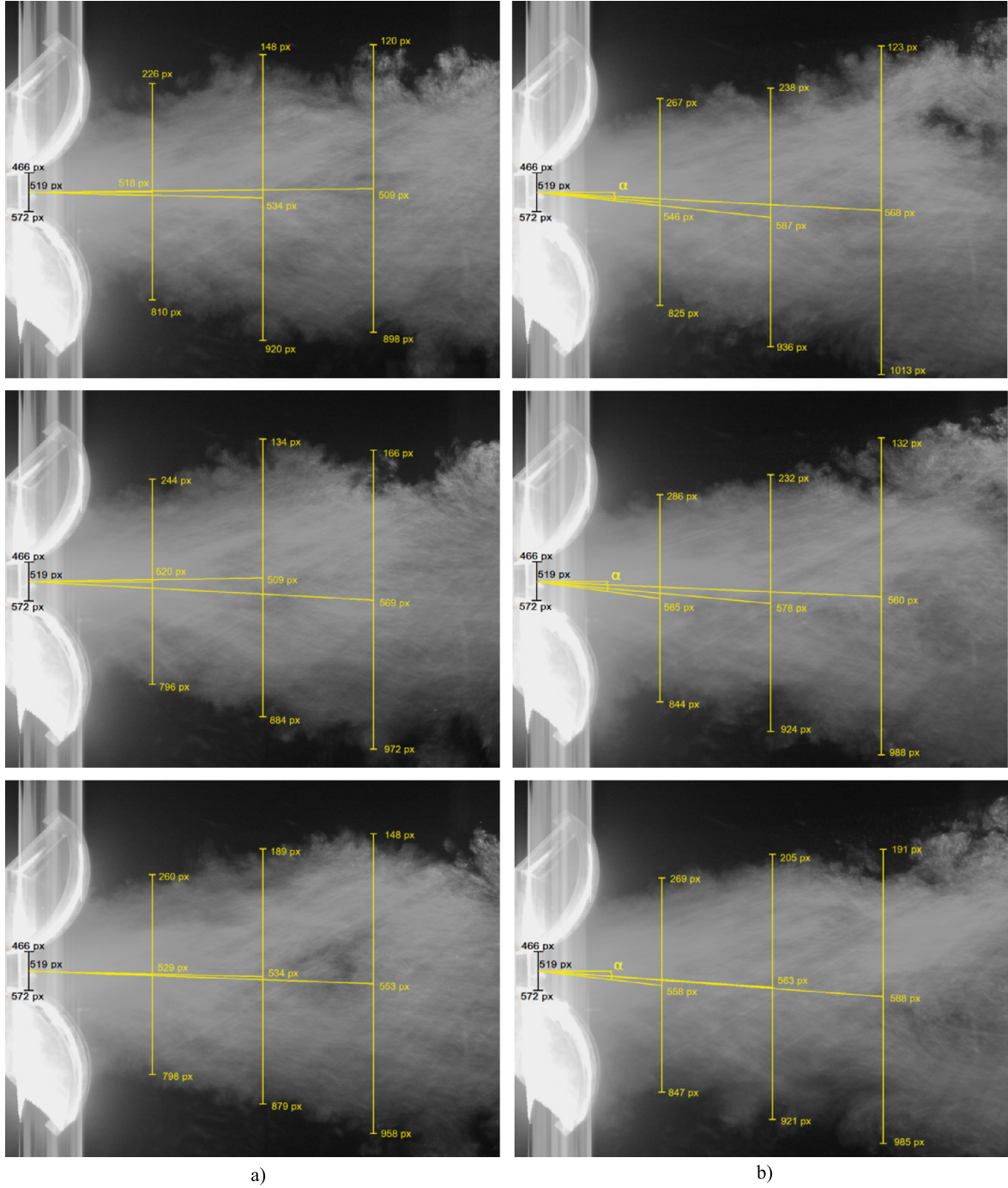


Fig. 15. Exit jet velocity angle at $V_R = 1$: a) DBD plasma off; b) DBD plasma on.

of a final result obtained by the mean of a series of measurements is given by the standard deviation of the mean ($\sigma_{\bar{x}}$). The standard deviation of the mean can be calculated by:

$$\sigma_{\bar{x}} = \left(\frac{1}{N(N-1)} \sum_{i=1}^N (x_i - \bar{x})^2 \right)^{1/2} \quad (13)$$

where x_i is the result of i th measurement, \bar{x} is the mean of the measurements and N is the number of measurements. Using the standard deviation of the mean, in the case with actuators off, the average angle is $0.687 \pm 0.056^\circ$ and the relative error is 9.18%. In the case with actuators on, the average angle is $4.86 \pm 0.23^\circ$ and the relative error is 4.93%. This is only an error in the sense

of obtaining averaged solution and not specifically an error of the measurement of flow field. The experimental results also confirm that when DBD actuators are active the flow is deflected.

Experimentally measured velocity angles for both cases, without plasma actuation and with plasma actuation with $V_R = 1$ corresponding to Fig. 15 are tabulated in Table 6. The random errors of the measurement process were estimated by the standard deviation of the mean error and are presented in Table 6. The results are actually an averaging procedure to obtain the steady average angle since the real flow is unsteady. Experimental results predict a lower value for the angle of deflection. As was mentioned before, these discrepancies between the computed and experimental results are ascribed to 3D effects existing in the experiment,

Table 3
Influence of single and double DBD plasma actuators on thrust and velocity angles.

		$(\alpha_T - \alpha_{0T})$	$(\alpha_V - \alpha_{0V})$		$(\alpha_T - \alpha_{0T})$	$(\alpha_V - \alpha_{0V})$
E01	1	8.40	6.12	E12	21.16	17.4
	1.5	0.04	−0.08		1.95	8.49
	2	0.26	1.30		0.68	3.28
E02	2.5	0.10	1.21	E23	0.04	4.59
	1	20.59	15.48		22.77	17.64
	1.5	1.36	1.82		5.80	8.79
E03	2	0.49	1.58	E34	1.57	3.46
	2.5	0.22	1.25		0.68	9.19
	1	1.71	0.24		2.01	0.43
E04	1.5	5.55	8.39	E45	6.17	9.41
	2	1.45	4.15		3.32	11.63
	2.5	0.51	3.29		1.11	9.49
E05	1	0.30	0	E56	0.09	0.00
	1.5	0.98	0.19		0.62	1.00
	2	2.70	7.95		3.36	11.89
E06	2.5	1.08	8.64	E67	0.96	17.51
	1	0.02	0		0.15	0.00
	1.5	−0.66	−0.48		−0.63	−0.44
E07	2	0.74	1.63	E67	0.52	1.70
	2.5	1.02	16.30		0.90	17.89
	1	0.05	0		0.11	0.00
E08	1.5	−1.08	−1.29	E67	−1.12	−1.34
	2	0.06	0.31		0.05	0.32
	2.5	0.12	0.93		0.12	0.93
E09	1	4.19	0.00			
	1.5	−1.18	−1.54			
	2	−0.01	0.01			
	2.5	0.00	0.11			

pure axial velocities as imposed boundary conditions in numerical experiments. Thus, it is to expect a high degree of deflection obtained by the numerical computation in comparison with the experimental and it was correctly expected that 2D exit model is “guiding” more directly the flow as compared to the 3D experiments. However, we should mention that although the experimental results are preliminary, the objective of the paper is not a direct numerical–experimental quantitative comparison. Instead the objective is to show through a qualitative comparison that numerical results could be used to confirm the possibility of using DBDs for thrust vectorizing and better designing the experimental tests.

6. Conclusions

Plasma actuators were used for controlling the flow over the Coanda surface of the ACHEON nozzle. When the plasma actuator is used, it was possible to postpone separation of the flow

Table 4
Influence of three DBD plasma actuators on thrust and velocity angle.

		$(\alpha_T - \alpha_{0T})$	$(\alpha_V - \alpha_{0V})$		$(\alpha_T - \alpha_{0T})$	$(\alpha_V - \alpha_{0V})$
E123	1	23.69	18.92	E1-4	23.90	19.10
	1.5	6.01	8.93		6.76	5.95
	2	1.66	4.57		3.47	9.08
E234	2.5	0.80	5.19	E1-5	1.12	11.22
	1	23.17	18.59		23.97	19.21
	1.5	6.54	11.04		6.88	6.17
E345	2	3.42	12.14	E1-6	3.76	11.95
	2.5	1.13	9.86		0.85	19.20
	1	1.81	2.04		23.92	19.23
E456	1.5	6.36	10.55	E1-7	6.84	6.10
	2	3.64	13.61		3.78	12.28
	2.5	0.93	−4.67		0.35	23.39
E567	1	0.05	0.00	E1-7	23.87	19.21
	1.5	0.64	1.15		6.83	6.07
	2	3.46	12.39		3.77	12.27
E567	2.5	0.75	20.01	E1-7	0.29	23.07
	1	0.20	0.00			
	1.5	−0.68	−0.46			
E567	2	0.51	1.68			
	2.5	0.91	17.87			

Table 5
Comparison of the average velocity magnitudes between the experimental and numerical results for the case without DBD at $V_R = 1$ and $V_2 \approx 2$ m/s.

Velocity profile	Average velocity from experiments (m/s)	Average velocity from numerical computations with $V_2 = 2$ m/s
Profile 1 (1 cm from the reference)	4.084	3.437
Profile 2 (2 cm from the reference)	4.175	3.869
Profile 3 (3 cm from the reference)	4.201	4.304
Profile 4 (4 cm from the reference)	4.251	4.733
Profile 5 (5 cm from the reference)	4.639	5.160

and increase the deflection angle of the exit jet of the nozzle. To find the optimum position of the actuators, seven DBD actuators in forward forcing mode were placed over the Coanda surface considering the numerically obtained separation points. Different combinations of the multiple DBD actuators were also used. Results show that when the actuator is placed slightly before the surface point, enhanced thrust vectorizing with the use of DBD actuator is achievable. Moreover, both single and multiple DBD actuators

Table 6
Comparison of numerical results with experimentally measured exit jet velocity angle.

		Mean angle (°)	Average angle of deflection (°)	Numerical result (°)
Without plasma actuators	First snapshot	$\alpha_V = -0.17$	$\alpha_V = 0.90$	$\alpha_V = 0.0$
		$\alpha_V = 1.36$		
		$\alpha_V = -0.61$		
	Second snapshot	$\alpha_V = 0.17$		
		$\alpha_V = -0.91$		
		$\alpha_V = 3.07$		
	Third snapshot	$\alpha_V = 1.72$		
		$\alpha_V = 1.36$		
		$\alpha_V = 2.09$		
With plasma actuators	First snapshot	$\alpha_V = 4.64$	$\alpha_V = 4.93$	$\alpha_V = 6.12$
		$\alpha_V = 6.13$		
		$\alpha_V = 3.01$		
	First snapshot	$\alpha_V = 7.86$		
		$\alpha_V = 5.32$		
		$\alpha_V = 2.52$		
	First snapshot	$\alpha_V = 6.68$		
		$\alpha_V = 3.98$		
		$\alpha_V = 4.23$		

were used in reverse operating mode and also single and multiple DBD plasma jets were used for increasing the thrust vectoring characteristic of the nozzle. Results have shown that utilization of DBD plasma actuators used in reverse mode will promote the separation on the surface, thus will force the exit jet of the nozzle to deflect toward the other Coanda surface. Although reverse DBD plasma actuators and DBD plasma jets were not tested for all the range of velocity ratios, we could expect that using a combination of these actuators and normal operational mode of DBD actuators will provide flexibility for controlling the flow direction. Preliminary results of the experiments were compared with the results of numerical simulation. We should note that it is difficult to fully compare the present 3D experimental results with result of 2D numerical simulation, since firstly, the numerical results are 2D approximations of the 3D experimental configuration and in the 3D experiments the flow, after exiting the nozzle starts to spread towards the lateral areas. Moreover, the imposed boundary conditions in numerical cases are pure axial velocities that differ from the ones of the experiments. However, the present experimental and numerical results are consistent in the sense of demonstrating the capabilities of the CFD to help to system design by avoiding a large number of experiments. Detailed experimental study of the effect of plasma actuators on thrust vectoring efficiency of ACHEON nozzle will be presented in future work.

Conflict of interest statement

We certify that there is no conflict of interest with any financial organization regarding the material discussed in the manuscript.

Acknowledgements

The present work was supported by C-MAST – Center for Mechanical and Aerospace Sciences and Technologies, FCT (Portuguese Foundation for Science and Technology) Research Unit No. 151. Part of the work was also supported by FP7, European project ACHEON, Grant No. 309041.

References

- [1] M. Abdollahzadeh, J.C. Páscoa, P.J. Oliveira, Two-dimensional numerical modeling of interaction of micro-shock wave generated by nanosecond plasma actuators and transonic flow, *J. Comput. Appl. Math.* 270 (2013) 401–416, <http://dx.doi.org/10.1016/j.cam.2013.12.030>.
- [2] M. Abdollahzadeh, J.C. Páscoa, P.J. Oliveira, Modified split-potential model for modeling the effect of DBD plasma actuators in high altitude flow control, *Curr. Appl. Phys.* 14 (2014) 1160–1170, <http://dx.doi.org/10.1016/j.cap.2014.05.016>.
- [3] ACHEON Project, (n.d.), acheon.eu/.
- [4] N. Benard, P. Braud, J. Pons, G. Touchard, E. Moreau, Quasi-steady and unsteady actuation by surface non-thermal plasma discharge for control of a turbulent round air jet, *J. Turbul.* 8 (49) (2007), <http://dx.doi.org/10.1080/14685240701656139>.
- [5] N. Benard, J. Jolibois, M. Fort, G. Touchard, E. Moreau, Control of an axisymmetric subsonic air jet by plasma actuator, *Exp. Fluids* 43 (2007) 603–616.
- [6] N. Benard, N. Balcon, E. Moreau, Jet flow control by dielectric barrier discharge – excitation by axisymmetric and flapping modes, in: 47th AIAA Aerosp. Sci. Meet., 2009, AIAA 2009-776, 17 pp.
- [7] H. Do, W. Kim, M.G. Mungal, M.A. Cappelli, Bluff body flow separation control using surface dielectric barrier discharges, *AIAA* 2007-939, 2007, 9 pp.
- [8] R.J. Durscher, S. Roy, Three-dimensional flow measurements induced from serpentine plasma actuators in quiescent air, *J. Phys. D, Appl. Phys.* 45 (2012) 035202, <http://dx.doi.org/10.1088/0022-3727/45/3/035202>.
- [9] D.V. Gaitonde, Analysis of plasma-based flow control mechanisms through large-eddy simulations, *Comput. Fluids* 85 (2013) 19–26, <http://dx.doi.org/10.1016/j.compfluid.2012.09.004>.
- [10] K.B. Ginn, S. Jenkins, D.M. Wells, N.M. Brent, Nozzle plasma flow control utilizing dielectric barrier discharge plasma actuators, *US* 2011/0048025 A1, 2011.
- [11] D. Greenblatt, M. Schulman, A. Ben-Harav, Vertical axis wind turbine performance enhancement using plasma actuators, *Renew. Energy* 37 (2012) 345–354, <http://dx.doi.org/10.1016/j.renene.2011.06.040>.
- [12] <http://clusterdem.ubi.pt/>, (n.d.).
- [13] I.H. Ibrahim, M. Skote, Simulations of the linear plasma synthetic jet actuator utilizing a modified Suzen–Huang model, *Phys. Fluids* 24 (2012) 113602, <http://dx.doi.org/10.1063/1.4767724>.
- [14] G. Ilieva, J. Páscoa, A. Dumas, M. Trancossi, MAAT – promising innovative design and green propulsive concept for future airship's transport, *Aerosp. Sci. Technol.* 35 (2014) 1–14, <http://dx.doi.org/10.1016/j.ast.2014.01.014>.
- [15] J. Jolibois, M. Forte, É. Moreau, Application of an AC barrier discharge actuator to control airflow separation above a NACA 0015 airfoil: optimization of the actuation location along the chord, *J. Electrostat.* 66 (2008) 496–503, <http://dx.doi.org/10.1016/j.elstat.2008.03.008>.
- [16] J. Kim, M. Nishihara, I.V. Adamovich, M. Samimy, S.V. Gorbato, F.V. Plivak, Development of localized arc filament RF plasma actuators for high-speed and high Reynolds number flow control, *Exp. Fluids* 49 (2010) 497–511, <http://dx.doi.org/10.1007/s00348-010-0819-y>.
- [17] R.R. Kleinman, D.J. Bodony, J.B. Freund, Shear-flow excitation mechanisms of recessed localized arc-filament plasma actuators, *Phys. Fluids* 22 (2010) 116103, <http://dx.doi.org/10.1063/1.3507317>.
- [18] I.B.V. Kopiev, N. Ostrikov, M. Zaitsev, V.I. Kopiev, S.G.V. Bityurin, A. Klimov, I. Moralev, Jet noise control by nozzle surface HF DBD actuators, *AIAA* 2011-911, 2011, 16 pp.
- [19] Y. Li, Y. Wu, M. Zhou, C. Su, X. Zhang, J. Zhu, Control of the corner separation in a compressor cascade by steady and unsteady plasma aerodynamic actuation, *Exp. Fluids* 48 (2009) 1015–1023, <http://dx.doi.org/10.1007/s00348-009-0787-2>.
- [20] J. Little, M. Nishihara, I. Adamovich, M. Samimy, High-lift airfoil trailing edge separation control using a single dielectric barrier discharge plasma actuator, *Exp. Fluids* 48 (2009) 521–537, <http://dx.doi.org/10.1007/s00348-009-0755-x>.
- [21] J. Little, K. Takashima, M. Nishihara, I. Adamovich, M. Samimy, Separation control with nanosecond-pulse-driven dielectric barrier discharge plasma actuators, *AIAA J.* 50 (2012) 350–365, <http://dx.doi.org/10.2514/1.J051114>.
- [22] E. Moreau, Airflow control by non-thermal plasma actuators, *J. Phys. D, Appl. Phys.* 40 (2007) 605–636, <http://dx.doi.org/10.1088/0022-3727/40/3/S01>.
- [23] S. Nagaraja, V. Yang, I. Adamovich, Multi-scale modelling of pulsed nanosecond dielectric barrier plasma discharges in plane-to-plane geometry, *J. Phys. D, Appl. Phys.* 46 (2013) 155205, <http://dx.doi.org/10.1088/0022-3727/46/15/155205>.
- [24] M. Trancossi, F. Rodrigues, J.C. Páscoa, A. Dumas, Preliminary design, set-up and testing of a plasma DBD actuator for boundary layer control, in: *Int. Conf. Eng., 27–29 November, Covilhã, University of Beira Inter., 2013*.
- [25] M. Samimy, M. Kearney-Fisher, J.-H. Kim, A. Sinha, High speed and high Reynolds number jet control using arc filament plasma actuators for noise mitigation and for flow and noise diagnostics, *AIAA* 2011-22, 2011, 19 pp.
- [26] A. Santhanakrishnan, J.D. Jacob, Flow control with plasma synthetic jet actuators, *J. Phys. D, Appl. Phys.* 40 (2007) 637–651, <http://dx.doi.org/10.1088/0022-3727/40/3/S02>.
- [27] A. Santhanakrishnan, D.A. Reasor, R.P. LeBeau, Characterization of linear plasma synthetic jet actuators in an initially quiescent medium, *Phys. Fluids* 21 (2009) 043602, <http://dx.doi.org/10.1063/1.3097004>.
- [28] D.M. Schatzman, F.O. Thomas, Turbulent boundary-layer separation control with single dielectric barrier discharge plasma actuators, *AIAA J.* 48 (2010) 1620–1634, <http://dx.doi.org/10.2514/1.J050009>.
- [29] J.S. Shang, S.T. Surzhikov, R. Kimmel, D. Gaitonde, J. Menart, J. Hayes, Mechanisms of plasma actuators for hypersonic flow control, *Prog. Aerosp. Sci.* 41 (2005) 642–668, <http://dx.doi.org/10.1016/j.paerosci.2005.11.001>.
- [30] J. Shin, S. Mahadevan, Forcing mechanisms in supersonic flow actuation achieved by direct-current surface glow discharge plasma, *Aerosp. Sci. Technol.* 15 (2011) 18–24, <http://dx.doi.org/10.1016/j.ast.2010.05.007>.
- [31] M.T. Shyam, S. Das, M. Abdollahzadeh, J.C. Páscoa, A. Dumas, Numerical modeling of Coanda effect in a novel propulsive system, *Int. J. Multiph. J.* 8 (2014) 181–201.
- [32] A.Y. Starikovskii, D.V. Roupasov, A.A. Nikipelov, M.M. Nudnova, Acoustic Noise and Flow Separation Control by Plasma Actuator, *AIAA* 2009-695, 2009, 28 pp.
- [33] K. Takashima (Udagawa), Y. Zuzek, W.R. Lempert, I.V. Adamovich, Characterization of a surface dielectric barrier discharge plasma sustained by repetitive nanosecond pulses, *Plasma Sources Sci. Technol.* 20 (2011) 055009, <http://dx.doi.org/10.1088/0963-0252/20/5/055009>.
- [34] J.R. Taylor, *An Introduction to Error Analysis: The Study of Uncertainties in Physical Measurements*, University Science Books, 1982.
- [35] M. Trancossi, A. Dumas, S.S. Das, J.C. Páscoa, Design methods of Coanda nozzle with two streams, *INCAS Bull.* 6 (2014) 83–95.
- [36] C.-C. Wang, S. Roy, Energy and force prediction for a nanosecond pulsed dielectric barrier discharge actuator, *J. Appl. Phys.* 111 (2012) 103302, <http://dx.doi.org/10.1063/1.4722202>.
- [37] C. Wang, S. Roy, Numerical simulation of a gas turbine combustor using nanosecond pulsed actuators, *AIAA* 2013-0894, 2013, 17 pp.
- [38] C. Wang, R. Durscher, S. Roy, Three-dimensional effects of curved plasma actuators in quiescent air, *J. Appl. Phys.* 109 (2011) 083305, <http://dx.doi.org/10.1063/1.3580332>.
- [39] C.M. Xisto, J.C. Páscoa, M. Abdollahzadeh, J.A. Leger, P. Masarati, L. Gagnon, et al., PECyt-plasma enhanced cyclodial thruster, in: *AIAA*, 2014, pp. 1–13.